JJMIE

Volume 8 Number 3, June. 2014
ISSN 1995-6665
Pages 127 - 136

Jordan Journal of Mechanical and Industrial Engineering

Numerical Study of the Hydrodynamic Structure of a Water Savonius Rotor in a Test Section

Ibrahim Mabrouki *, Zied Driss , Mohamed Salah Abid

Laboratory of Electro-Mechanic Systems (LASEM), National School of Engineers of Sfax (ENIS), University of Sfax, B.P. 1173, Road Soukra km 3.5, 3038 Sfax, TUNISIA.

Received 18 Feb 2014 *Accepted 18 Jun 2014*

Abstract

Turbulent free surface flows are encountered in many hydraulic and water resources engineering problems. Their understanding is thus a critical prerequisite for designing stream and river restoration projects and a broad range of hydraulic structures. For this purpose, a volume of fluid (VOF) advection algorithm, coupled with the Reynolds averaged Navier-Stokes (RANS) equations with a two-equation turbulence closure model, is employed. For efficiently describing and predicting the degree of turbulence in dam-break flows, the computations are carried out with the variation of initial turbulence intensities. From this investigation, it was found that the power performances of a Savonius water turbine were changed with the distance between the rotor and the bottom wall of the tunnel and with a rotation direction of the rotor.

Keywords: *CFD, VOF, Turbulence, Hydrodynamic, Savonius Rotor, Water Turbine*

1. Introduction

The Savonius vertical axis water turbine is simple in structure, has good starting characteristics, relatively low operating speeds, and an ability to accept water from any direction. However, has a lower efficiency than some other vertical axis water turbines. So far a number of experimental investigations have been carried out to study the performance of the Savonius rotor. Due to the problems of the conventional sources of energy, like the depletion of its resources and environmental pollutions, great efforts are made towards the use of renewable energy sources. Hydraulic energy is considered one of the most important renewable energy sources because of its availability, simplicity and economy. Water rotors are the main tools of hydraulic energy. Savonius water rotor is one of the simplest and cheapest vertical axis water turbines. It is constructed from two vertical half cylinders and has good starting characteristics, relatively low operating speeds and ability to capture water from any direction. In fact, the performance of Savonius rotor has been widely studied by many researchers in order to determine its optimum design parameters. The effect of the blade aspect ratio, the blade overlap, the end plates, and the shielding were tested by Alexander and Holownia [1]. They concluded that there was an improvement in the rotor performance after increasing the aspect ratio and rotor overlap ratio. The tests of three and four bladed geometries gave appreciably lower values of efficiency than the two blades rotor. Roth [2] and Modi *et al.* [3] reported that the optimum values of aspect and overlap ratios are 0.77 and 0.25, respectively. Mojola [4] concluded that the effect of overlap ratio on rotor performance depends on its tip speed ratio. Most of hydropower is generated by a large-scale hydroelectric plant. Some have suggested that dam constructions can lead to tremendous environmental damages. On the other hand, small/micro/nano hydropower has attracted much attention in the recent years mainly because of the decrease of construction place for large-scale plants and environmental conservation.

There have been many studies on a Savonius wind rotor, e.g., rotor configurations, a flow field around rotor numerical simulations and others [5]. The advantages of Savonius rotor using for the hydropower are little complex constitution, low cost, durability and easy maintenance. Although the previous studies give us useful information, problems of Savonius hydraulic turbine, used for the hydropower, are still unclear [6]. Fujisawa and Gotoh [7] have conducted experimental studies by flow visualization techniques, such as smoke wires. The studies of the smoke-wire method revealed variations in the flow around the rotor with rotor angle, but only qualitative information could be obtained. Measurements of the pressure distribution on the blade surfaces were carried out by Fujisawa [8], which provided some help in understanding the flow phenomena revealed by the flow visualization studies.

According to these anterior studies, there is a lack of detailed descriptions of the field for different types of Savonius rotors. Thus, the present paper aims at numerically exploring the three-dimensional unsteady flow

* Corresponding author. e-mail: : mabroukiibrahim@hotmail.fr.

over a conventional Savonius type rotor. It is thought that this approach could lead to a cheaper power generation without the environmental disruptions, compared with that produced by the large-scale hydroelectric plant.

2. Numerical Model

2.1. Geometrical Arrangement

Figure 1 shows the geometrical arrangement of the test section bench with an obstacle. The water turbine is placed on the test section at the point defined by x=4 m, y=-0.8 m and z=0.7 m. In these conditions, the test section is reduced from L_1= 0.4 m to L_2= 0.2 m. The turbine is equipped by two cylindrical buckets with a height equal to H=0.1 m and a diameter D= 0.1 m.

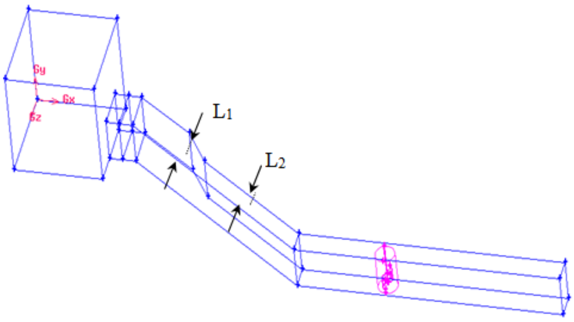

Figure 1. Geometrical arrangement.

2.2. Meshing

Figure 2 presents the meshing of the test bench with obstacle. It consists of 170426 nodes and 924170 cells. A tetrahedral hybrid is used as a type of cells for the meshing.

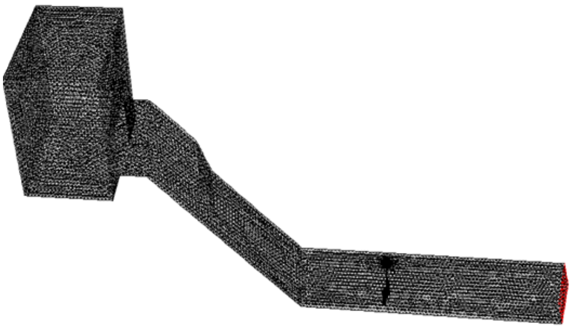

Figure 2. Meshing.

2.3. Boundary Condition

Figure 3 illustrates the boundary conditions using the commercial CFD code "FLUENT". The control volume, consisting of the intake, the penstock and the test section, is limited by "wall" condition. The control gate, located at the outlet of the intake, is modelized by an interior surface which will be removed at the instant t=0 s to start the water flow through the test bench. However, we impose the out flow condition in the test section. For the turbine, we have used the MRF model in order to approach the hydrodynamic behavior. A rotative speed equal to 500 rpm is imposed.

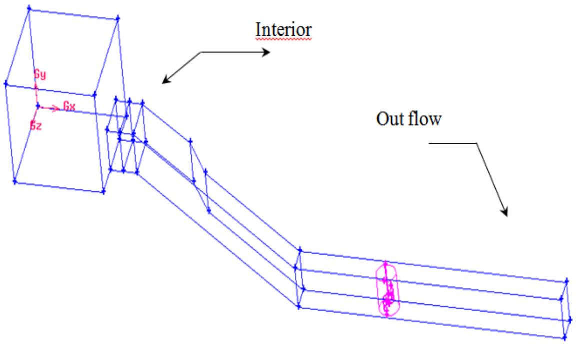

Figure 3. Boundary conditions.

2.4. MRF Model

The Multiple Reference Frame (MRF) model is the simplest of the three approaches for modeling problems that involve both stationary and moving zones. It is a steady-state approximation in which individual cell zones move at different rotational speeds. This approach is appropriate when the flow, at the boundary between these zones, is nearly uniform. While the multiple reference frame approach is clearly an approximation, it can provide a reasonable model of the time-averaged flow for many applications. When the relative velocity formulation is used, velocities in each sub domain are computed relative to the motion of the sub domain. Velocities and velocity gradients are converted from a moving reference frame to the absolute inertial frame as described below.

The position vector relative to the origin of the zone rotation axis is defined as:

$$\vec{r} = \vec{x} - \overrightarrow{x_0} \tag{1}$$

Where $\vec{x}$ is the position in absolute cartesian coordinates and $\overrightarrow{x_0}$ is the origin of the zone rotation axis. The relative velocity in the moving reference frame can be converted to the absolute (stationary) frame of reference using the following equation:

$$\vec{v} = \vec{v}_r + (\vec{\omega} \times \vec{r}) + \vec{v}_t \tag{2}$$

Where $\vec{v}$ is the velocity in the absolute inertial reference frame, $\vec{v}_r$ is the velocity in the relative non inertial reference frame, and $\vec{v}_t$ is the translational velocity of the non inertial reference frame.

Using this definition of absolute velocity, the gradient of the absolute velocity vector is given by:

$$\nabla\vec{v} = \nabla\vec{v}_r + \nabla(\vec{\omega} \times \vec{r}) \tag{3}$$

3. Mathematical Formulation

3.1. Navier Stocks Equations

The governing equations for a Newtonian fluid are:

Conservation of Mass:

$$\frac{\partial \rho}{\partial t} + \frac{\partial \rho \bar{U}_i}{\partial x_i} = 0 \tag{4}$$

Conservation of momentum:

$$\frac{\partial \rho \tilde{u}_i}{\partial \tau} + \frac{\partial \rho \tilde{u}_j \tilde{u}_i}{\partial x_j} = \frac{\partial}{\partial x_j}\left(\mu \frac{\partial \tilde{u}_i}{\partial x_j}\right) - \frac{\partial \tilde{p}}{\partial x_i} + \rho g_i + \tilde{s}_{ui} \quad (5)$$

Where:
ρ: Density of fluid.
τ : Viscous stress.
u_i: Cartesian component of velocity in the direction x_i.
μ: Molecular kinematic viscosity.
k: Turbulent kinetic energy.
g_i: Gravitational acceleration.

The turbulent flow field is characterized by velocity fluctuations in all directions and has an infinite number of scales (degrees of freedom). Solving the Navier–Stocks equations for a turbulent flow is impossible because the equations are elliptic, non-linear and coupled (pressure-velocity, temperature-velocity). One of the solutions is to reduce the number of scales by using the Reynolds decomposition. Any property (whether a vector or a scalar) can be written as the sum of an average and a fluctuation:

$$\tilde{\emptyset} = \Phi + \emptyset \quad (6)$$

where the capital letter denotes the average and the lower case letter denotes the fluctuation of the property. Of course, this decomposition will yield a set of equations governing the average flow field. The new equations will be exact for an average flow field, not for the exact turbulent flow field. By an average flow field, we mean that any property becomes constant over time. The result of using Reynolds decomposition in the Navier–Stocks equations is called the Reynolds Averaged Navier Stokes equations (RANS). For each variable, we substitute the corresponding decomposition and we obtain the following RANS equations upon substitution of the Reynolds decomposition.

3.2. Standard k-ε Model

The standard k-ε model, developed by Launder and Spalding, is a two-equation eddy viscosity turbulence model. In this model, the turbulent viscosity is computed based on the turbulence kinetic energy k, and the turbulence dissipation rate ε:

$$\mu_t = C_\mu \frac{k^2}{\varepsilon} \quad (7)$$

Each of these two turbulence scales has its transport equation. The turbulence kinetic energy equation k is derived from the exact momentum equation by taking the trace of the Reynolds stress. This equation can be expressed as:

$$\frac{\partial k}{\partial t} + \bar{u}_i \frac{\partial k}{\partial x_i} = \nu_t \left[\frac{\partial \bar{u}_i}{\partial x_j} + \frac{\partial \bar{u}_j}{\partial x_i}\right]\frac{\partial \bar{u}_i}{\partial x_j} + \frac{\partial}{\partial x_i}\left(\frac{\nu_t}{\sigma_k}\frac{\partial k}{\partial x_i}\right) - \varepsilon \quad (8)$$

The dissipation rate equation, on the other hand, is obtained using physical reasoning. This equation can be expressed as:

$$\frac{\partial \varepsilon}{\partial t} + \bar{u}_i \frac{\partial \varepsilon}{\partial x_i} = C_{\varepsilon 1} \frac{\varepsilon}{k} \nu_t \left[\frac{\partial \bar{u}_i}{\partial x_j} + \frac{\partial \bar{u}_j}{\partial x_i}\right]\frac{\partial \bar{u}_i}{\partial x_j} + \frac{\partial}{\partial x_i}\left(\frac{\nu_t}{\sigma_\varepsilon}\frac{\partial \varepsilon}{\partial x_i}\right) - C_{\varepsilon 2} \frac{\varepsilon^2}{k} \quad (9)$$

These values were obtained using experiments and computer optimization. It is worth noting that these values are not universal and the k-ε model requires some amount of fine tuning in order to obtain correct results.

3.3. Volume of Fluid (VOF)

If one defines motions of the interface using a volume fraction field, the resulting VOF equation is described as:

$$\frac{\partial}{\partial t}\int_{\Omega} \alpha \, d\Omega + \int_{S} \alpha v . ndS = 0 \quad (10)$$

Here, the density and viscosity are determined on the basis of the level-set function as:

$$\rho(\phi) = H(\phi)\rho_l + (1\text{-}H(\phi))\ \rho_g \quad (11)$$

$$\mu(\phi) = H(\phi)\ \mu_l + (1\text{-}H(\phi))\ \mu_g \quad (12)$$

Where the subscripts l and g denote the liquid and the gas respectively, ρ is the density, μ is the molecular kinematic viscosity. If the level-set construction process for considering surface tension effects is unnecessary, the local density and viscosity of the fluid can be defined using the volume fraction instead of the level-set function as follows:

$$\rho(\alpha) = \alpha\rho_l + (1\text{-}\alpha)\ \rho_g \quad (13)$$

$$\mu(\alpha) = \alpha\mu_l + (1\text{-}\alpha)\ \mu_g \quad (14)$$

Instead of the ULTIMATE-QUICKEST scheme, which is used in the CICSAM for the boundedness of the volume fraction distribution, we propose a less complicated and lower-order scheme $2\tilde{\alpha}_D = \tilde{\alpha}_f$, that is one basis element of the HRIC's bounded DD scheme. After enforcing the CBC for explicit flow calculations blended with the Hyper-C scheme, the proposed high resolution scheme can be rewritten as follows:

$$\tilde{\alpha}_{f\,(HRIC)} = \begin{cases} \min(\tilde{\alpha}_D C_0 + 2\,\tilde{\alpha}_D\ (1 - C_0), \\ \quad \tilde{\alpha}_D \\ \quad \tilde{\alpha}_{f\,(Hyper-C)}) & \text{where } 0 \le \tilde{\alpha}_D \le 1 \\ & \text{elsewhere} \end{cases} \quad (15)$$

To achieve the balance between the smoothness and sharpness of the interface, we need a blending function that switches gradually between the Hyper-C and our proposed high resolution scheme. For this, we implement the following weighting factor, which is based on the orientation of the interface and the flow direction:

$$\gamma_f = \cos^4(\theta_f) \quad (16)$$

Where:

$$\theta_f = \arccos\left|\frac{(\nabla\alpha)_f . n_f}{|(\nabla\alpha)_f|\,|n_f|}\right| \quad (17)$$

n_f is the vector connecting the centers of the CV, D and A. We use a blending function of higher degree than in the CICSAM. This is defined as:

$$\gamma_f = 0.5(\cos(2\theta_f) + 1) = \cos^2(\theta_f) \quad (18)$$

  - Volume 8, Number 3 (ISSN 1995-6665)

The normalized cell face value for the volume fraction computed by using the proposed high resolution advection scheme is defined as:

$$\tilde{\alpha}_f = \gamma_f \tilde{\alpha}_{f\,(Hyper-C)} + (1-\gamma_f)\tilde{\alpha}_{f\,(HRIC)} \quad (19)$$

4. Numerical Results

4.1. Volume Fraction

Figure 4 presents the distribution of the volume fraction of water for the test section bench with obstacle in the x-y plane. According to these results, a decrease of the water height in the intake during the flow was noticed. The impact of water front with the turbine is very aggressive. In fact, this impact is due to the higher flow velocity created through the penstock. Also, the water front applies an important strength on the turbine blade, which is converted to the important torque and it becomes able to start the rotative motion of the turbine. In these conditions, the behavior of the water around the turbine can be observed at the instant t=1.504 s, which is characterized with an important turbulence phenomena.

4.2. Average Velocity

Figure 5 presents the average velocity in the x-z plane of the test bench section with obstacle, for different instances of the water flow. According to these results, it has been observed that the average velocity has a very week value in the intake during the flow. When the water flow ahead’s through the penstock until the turbine, an increase of the velocity distribution is observed. A wake zone was created near the turbine during the flow and it reaches a higher value after impacting the water turbine. In addition, a gradient of velocity appeared between the two blades of the turbine. The velocity gradient increases in value especially at the instance t=1.504 s. Also, it has been noted that the aim of air is located in the roof of the penstock and the test section. The velocity value increases with the ahead of water through the test section.

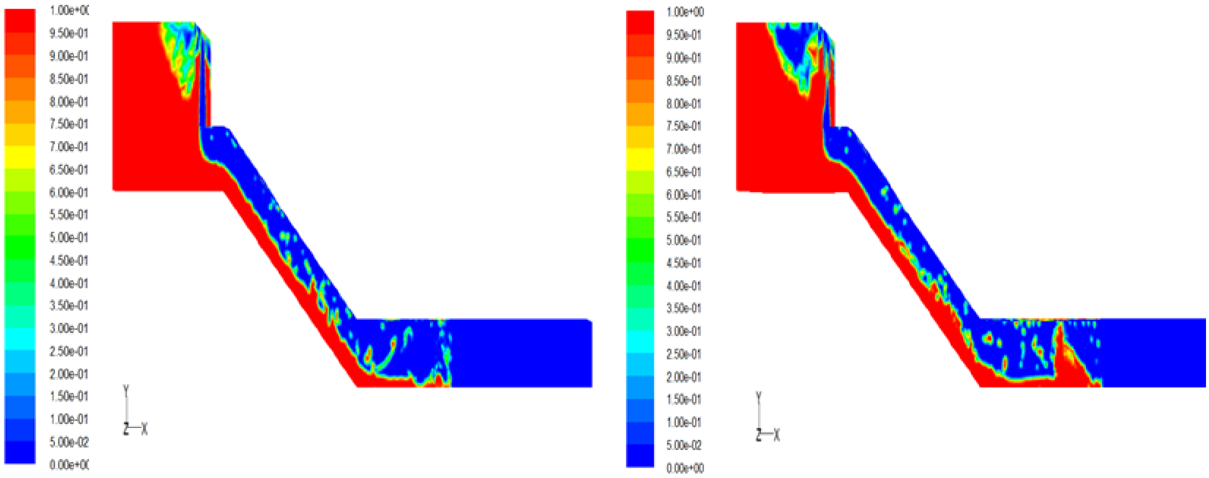

(a) t=1.411 s (b) t=1.504 s

Figure 4. Distribution of the volume fraction in the x-y plane

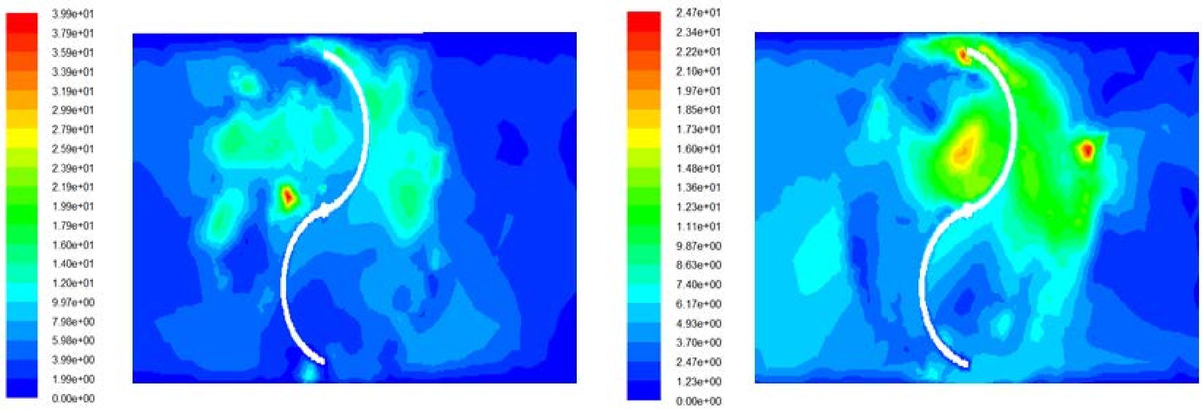

(a) t=1.411 s (b) t=1.504 s

Figure 5. Distribution of the average velocity in the x-z plane

4.3. Velocity Vectors

Figures 6 and 7 present the distribution of the velocity vectors in the test section bench in the x-y plane, and around the turbine in the x-z plane, for different instances of water flow. According to these results, it has been noted that the flow velocity is very weak in the intake. A circulation zone of the air was created in the upstream of the turbine. Indeed, the water's velocity increases near and around the turbine. This fact is due to the turbulence phenomena, which decrease in the turbine downstream.

4.4. Static Pressure

Figures 8 and 9 show the distribution of the static pressure in the test bench with obstacle in the x-y plane, and around the turbine in the x-z plane. In these condition, it has been noted that the static pressure is mesured relatively to the atmospherique pressure. According to these results, it has been noted that the static pressure has a uniforme value through the test bench section. Also, the static pressure value has a weak value. This fact can ameliorate the hydrodynamic behavior of the test bench section. In addition, a compression zone located near the blade of the turbine buckets has been observed. The compression zone has an important value when the water flow impacts the turbine at t=1.411 s. However, it decreases the ahead of the water front through the test section. The zone around the turbine has a uniforme value, which is very important. In fact, the increase of the static pressure is due to the rotation velocity of the turbine.

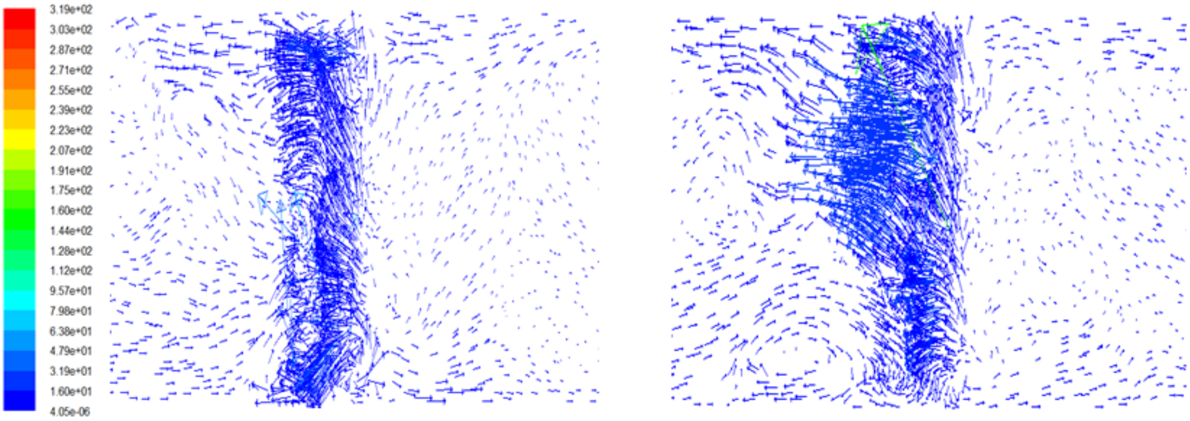

(a) t=1.411 s (b) t=1.504 s

Figure 6. Distribution of the velocity vectors in the x-y plane.

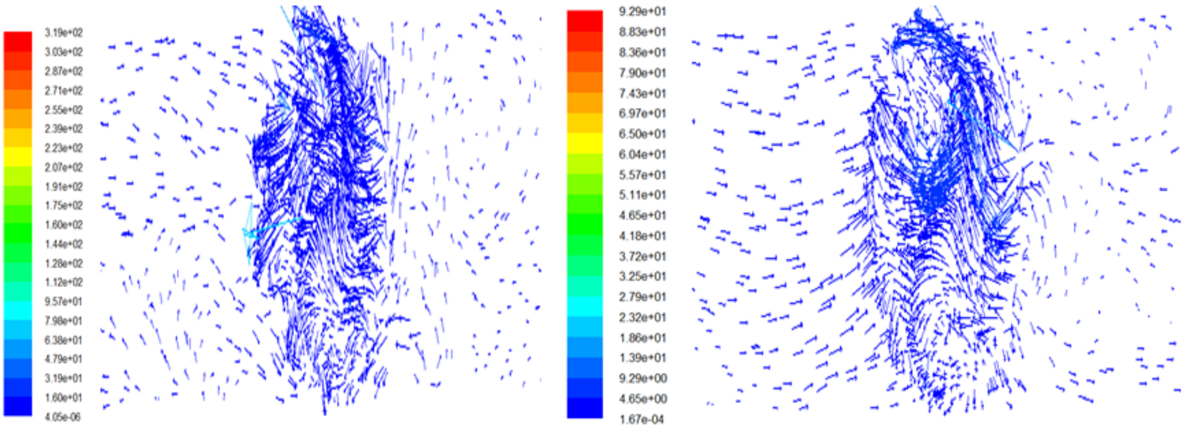

(a) t=1.411 s (b) t=1.504 s

Figure 7. Distribution of the velocity fields in the x-z plane.

  - Volume 8, Number 3 (ISSN 1995-6665)

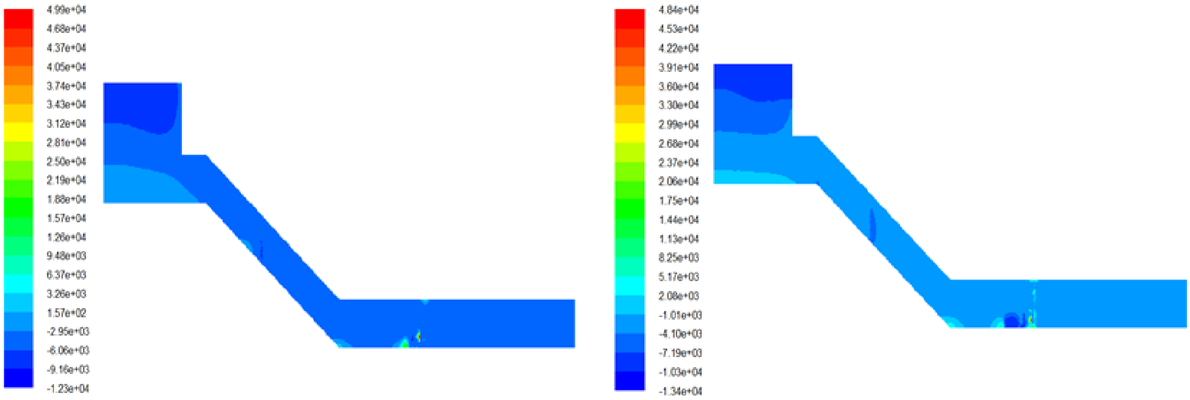

(a) t=1.411 s (b) t=1.504 s

Figure 8. Distribution of the static pressure in the x-y plane.

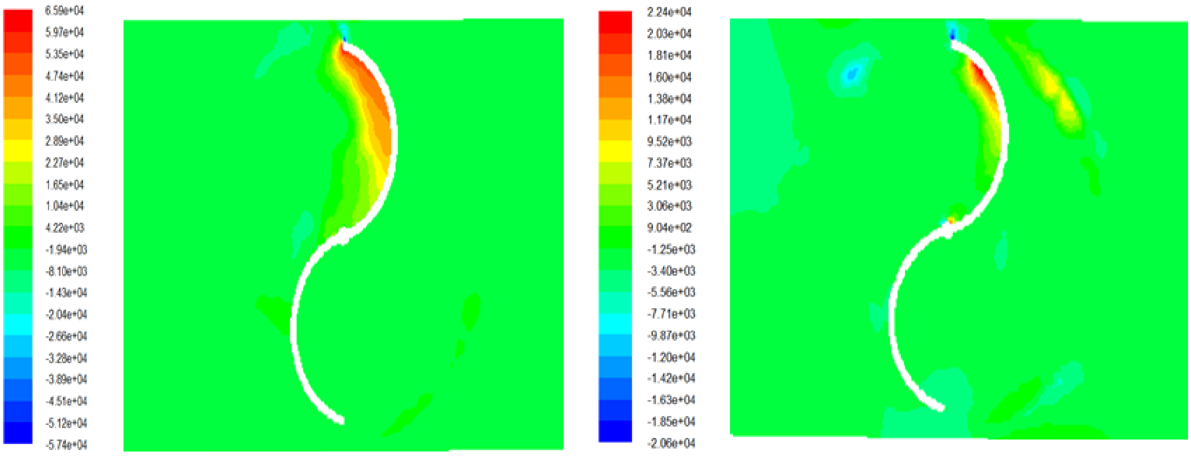

(a) t=1.411 s (b) t=1.504 s

Figure 9. Distribution of the static pressure in the x-z plane.

4.5. Dynamic Pressure

Figure 10 shows the distribution of the dynamic pressure on the test bench section in the x-z plane for different instances of the flow. According to these results, it has been noted that the dynamic pressure is uniform in the intake and in the penstock at t=1.504 s. It increases after impacting the turbine. A compression zone was created near the blade of the turbine. This zone increases in value and area extension, after the water flows ahead through the turbine. The maximum value of dynamic pressure reaches p=94800 Pa, which is able to put the turbine on rotation motion. Indeed, it has been noted that the zone around the turbine has an important value. In fact, the penstock ameliorates the water flow behavior of the turbine.

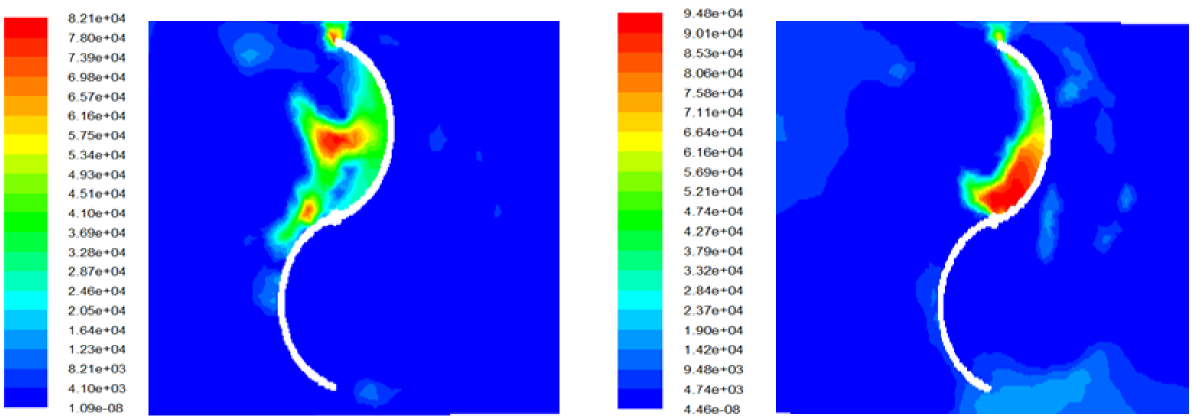

(a) t=1.411 s (b) t=1.504 s

Figure 10. Distribution of the dynamic pressure in the x-z plane.

4.6. Turbulent Kinetic Energy

Figure 11 shows the distribution of the turbulent kinetic energy for the test section bench with obstacle in the x-z plane. According to these results, it has been noted that the turbulent kinetic energy is uniform in the penstock and the test section. However, a wake zone characteristic of the maximum values appears around the turbine. This zone is located between the upstream and the downstream of the turbine during the water flow. The zone extension decreases during the ahead of the water flow through the test section.

4.7. Turbulent Dissipation Rate

Figure 12 shows the distribution of the turbulent dissipation rate in the test section bench with obstacle in the x-z plane. According to these results, it has been noted that the turbulent dissipation rate presents the same distribution with those of the turbulent kinetic energy. Indeed, a very low value of the turbulent dissipation rate in the penstock and in the test section has been observed. This value is uniform in the flow field. However, a variation of the turbulent dissipation rate values appears around the turbine. This fact is due to the turbulence phenomena created around the turbine and the friction of water with the wall of the test section bench.

4.8. Turbulent Viscosity

Figure 13 presents the behavior of the turbulent viscosity in the test section bench in the x-y plane and around the turbine in the x-z plane for diffenrent instances of water flow. According to these results, wake zone characteristics of the maximum values of the turbulent viscosity appear in the middle of the intake, which decreases in value during the flow. Also, the variation of the turbulent viscosity has been observed near the turbine bucket. At t=1.504 s, a wake zone, located in the downstream of the turbine, has been observed, with a maximal value equal to 6.64 Pa.s.

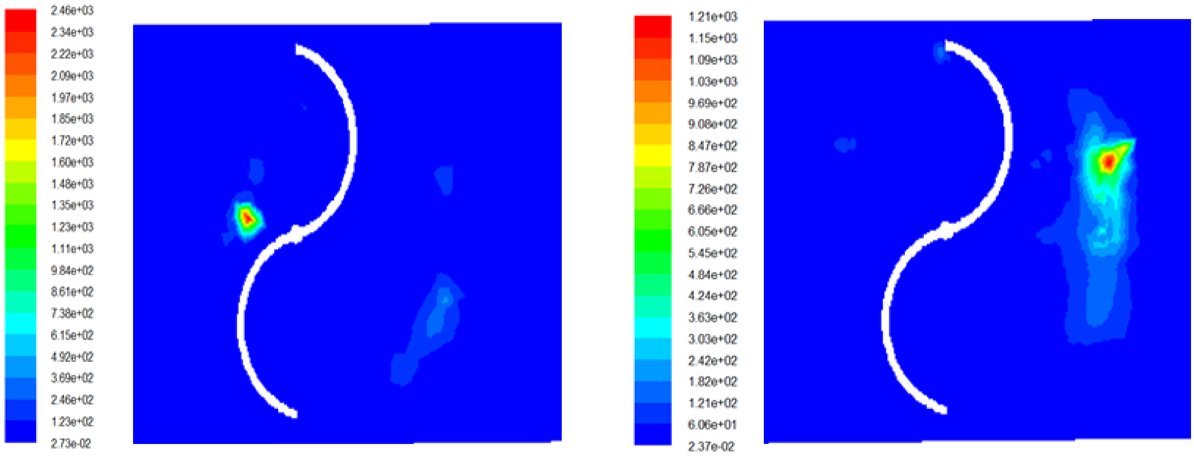

(a) t=1.411 s (b) t=1.504 s

Figure 11. Distribution of the turbulent kinetic energy in the x-z plane.

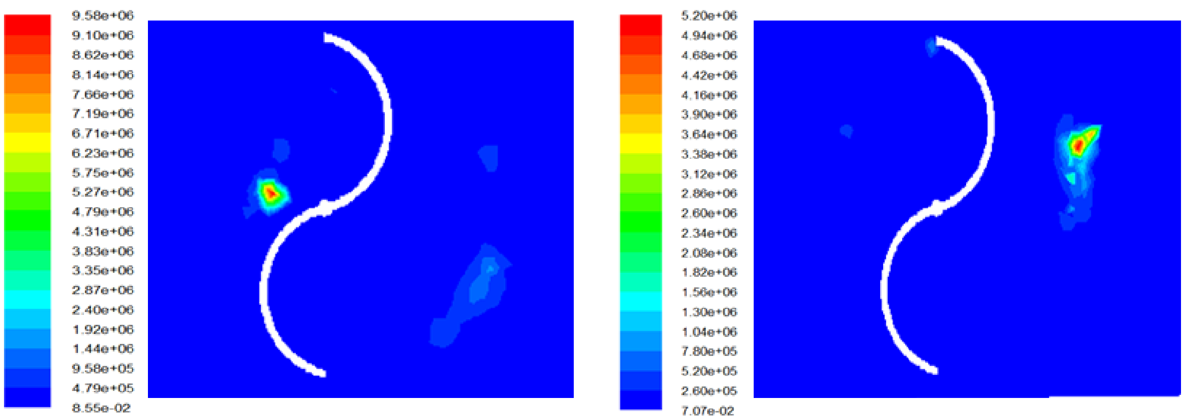

(a) t=1.411 s (b) t=1.504 s

Figure 12. Distribution of the turbulent dissipation rate in the x-z plane.

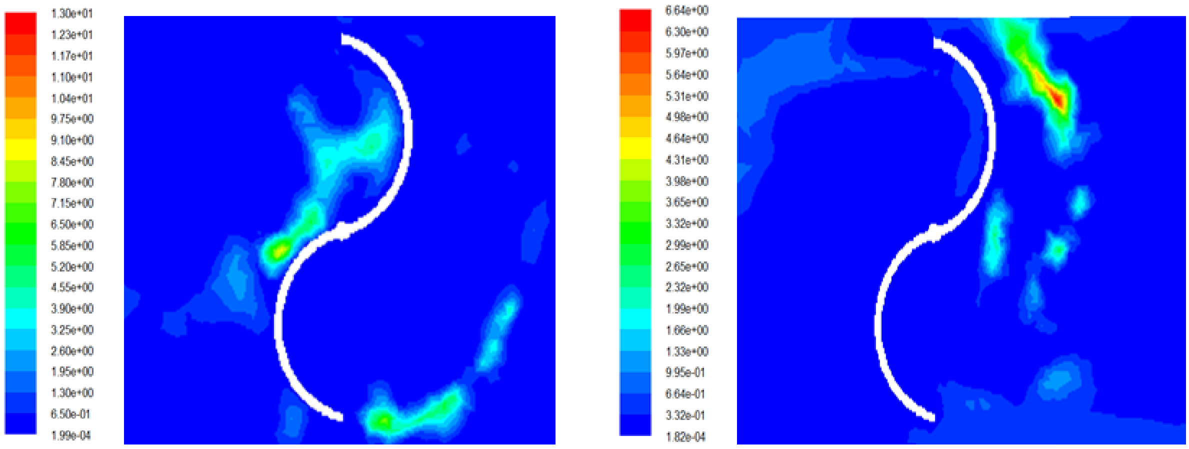

(a) t=1.411 s (b) t=1.504 s

Figure 13. Distribution of the turbulent viscosity in the x-z plane.

4.9. Vorticity

Figure 14 shows the distribution of vorticity in the test section bench in the x-z plane for different instances of flow. According to these results, it has been noted that the value of vorticity is uniform along the penstock and the test section, and it is very low during the water flow. However, a wake zone characterictics of the maximum values of the vorticity appear around the turbine.

4.10. Comparaison with Experimental Results

Figures 15 and 16 compare the numerical results obtained by the commercial CFD code "FLUENT", for the test section bench with obstacle and equipped with turbine, with the experimental results obtained from the test section bench. The comparison between the numerical and the experimental results consists on the curves which present the free surface and the water front of the flow. According to these results, the ahead of the flow through the test section and the impact between the water front and the turbine has been observed. The comparaison was carried out for the validation of our numerical model for these cases. In fact, the comparaison shows an acceptable aggrement between the experimental and the numerical results. The gap between the results is about 6%.

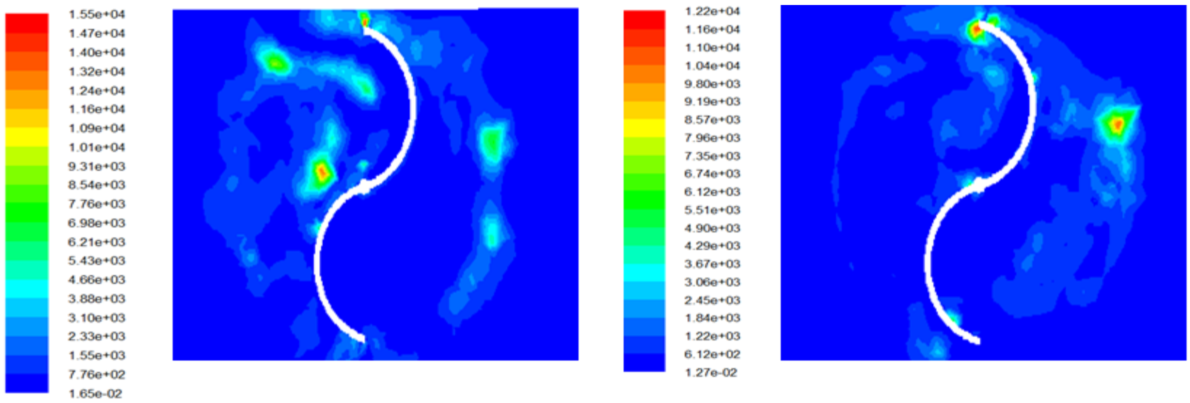

(a) t=1.411 s (b) t=1.504 s

Figure 14. Distribution of the vorticity in the x-z plane.

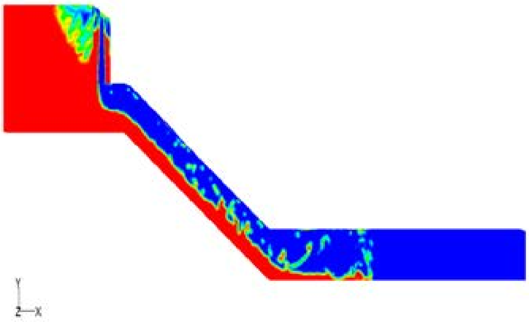

(a) Numerical

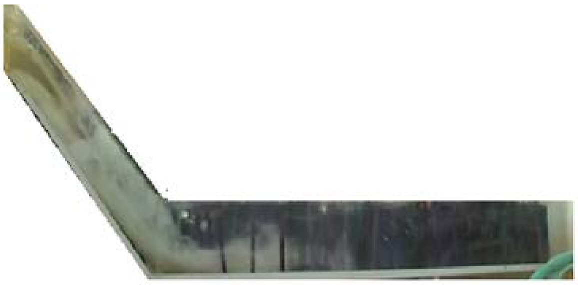

(b) Experimental

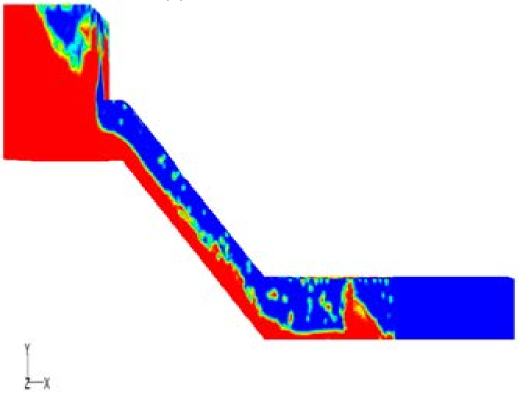

(c) Numerical

(d) Experimental

Figure 15. Comparison of the volume fraction with experimental results.

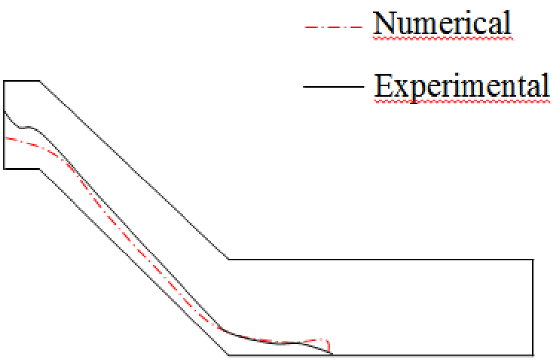

(a) t=1.411 s

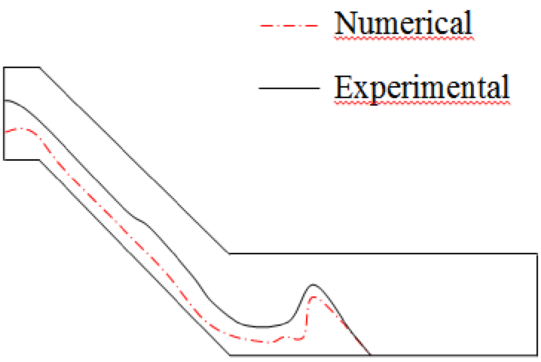

(b) t=1.504 s

Figure 16. Comparaison between numerical and experimental results.

5. Conclusion

The present study explored the non-linear of three dimensional unsteady potential flows over water Savonius rotor to hopefully develop a simulation method for predicting its hydrodynamic performance. The performance of cross-flow water turbines of the Savonius type, for very low head hydropower applications, has been investigated after the CFD model validation. A model of a water Savonius turbine was constructed and tested in a water tunnel to arrive at an optimum installation condition. A flow field around the rotor was examined visually to clarify the influences of the installation conditions on the flow field. The flow visualization showed a difference in the flow pattern around the rotor by changing these parameters. A decrease in the water height in the intake during the flow has been observed. The impact of water front with the turbine was very aggressive. This fact is due to the higher flow velocity created through the penstock. The velocity was increased in value simultaneously with the ahead of water through the water channel. Also, it has been noted that the turbulent of dissipation rate is due to the turbulence phenomena created around the turbine and the friction of water with the wall of the test section bench.

Acknowledgments

The authors would like to thank the Laboratory of Electro-Mechanic Systems (LASEM) members for financial assistance.

References

[1] Alexander, A.J., Holownia, B.P., Wind tunnel tests on a Savonius rotor. Journal of Industrial Aerodynamics 3(1978), 343-351.

[2] Roth, N.J, Prototype design and performance of Savonius rotor based on irrigation system (Thesis of Master Degree) University of British Columbia, 1982.

[3] Modi, V.J., Roth, N.J., Fernando, M.S, Optimum-configuration studies and prototype design of a wind-energy-operated irrigation system. Journal of Wind Engineering and Industrial Aerodynamics 16 (1984), 85-96.

[4] Mojola, O., on the aerodynamic design of the Savonius windmill rotor. Journal of Wind Engineering and Industrial Aerodynamics 21(1985), 223-231.

[5] Bergeles, G. and Athanassiadis, On the Flow Field around a Savonius Rotor, Wind Engineering, Vol.6 (1982) No.3 140-148.

[6] Ueno, H., Mino, M. and Takada, N., Savonius type wind turbine, Influence of a side plate, Journal of Japan Solar Energy Society (2002) 35-40.

[7] Fujisawa N, Gotoh F. Visualization study of the flow in and around a Savonius rotor, Experiments in Fluids, 407-412, 1992.

[8] Fujisawa N, On the torque mechanism of Savonius rotors, Journal of Wind Engineering and Industrial Aerodynamics, 277-292, 1992.

[9] Fujisawa, N. and Taguchi, Y, Investigation of Flow Field around Savonius Rotors by Particle Imaging Velocimetry and Numerical Calculations, Turbo machinery, 439-447, 1995.

[10] J. Fluid Mech. 374, 407-424.

[11] Whitham, G.B, The effects of hydraulic resistance in the dam break problem. Proc. R. Soc. London, 399-407, 1955.

[12] Violeau, D., Issa, R. Numerical modeling of complex turbulent free-surface flows with the SPH method: an overview. Int. J. Numer. Methods Fluids 53 (2007), 277-304.

[13] I. Mabrouki, Z. Driss, and MS. Abid, “Experimental validation on the flow around a water Savonius rotor,” Troisième Congrès Tunisien de Mécanique, COTUME’2014.